Energy & Environmental Science

Broadening solid ionic conductor selection for sustainable and earth-abundant solid-state lithium metal batteries

Journal:	*Energy & Environmental Science*
Manuscript ID	EE-ART-08-2023-002657.R1
Article Type:	Paper
Date Submitted by the Author:	26-Sep-2023
Complete List of Authors:	Zou, Peichao; University of California Irvine, Physics and Astronomy Wang, Chunyang; University of California Irvine, Physics and Astronomy He, Yubin; UC Irvine Xin, Huolin; University of California Irvine, Physics and Astronomy

Broader context statement

In the past half a century, a host of solid ionic materials, i.e., garnets, (anti)perovskites, halides, sulfides, NASICONs, were discovered for conducting lithium ions. Most of them are unstable towards lithium metal anodes. The rare materials that have a cathodic stability window down to 0 V (vs. Li/Li^+) are garnet materials, which yet contain lanthanum (La), a rare earth element and critical material. We know that there are a handful of battery anode materials that are reasonable Li-ion conductors, constitute only earth-abundant materials, and can be discharged to 0 V (vs. Li/Li^+) without large volume expansion and phase conversion. However, there are rare reports using these electrode materials as solid electrolytes, because these materials typically have electronic conductivities that are orders of magnitude higher than that required for solid electrolytes. Here, we leverage a simple sandwich-type solid electrolyte architecture design to enable any ceramic lithium-ion conductors to be deployed in solid-state batteries, and the requirements of electronic insulation or (electro)chemical stability for the ceramic lithium-ion conductors are no longer needed. With our solid electrolyte design, a broad range of ionic conductors, including lithium battery electrode materials, has been applied in solid-state lithium metal batteries with superior cycle life.

ARTICLE

Broadening solid ionic conductor selection for sustainable and earth-abundant solid-state lithium metal batteries

Received 00th January 20xx,
Accepted 00th January 20xx

DOI: 10.1039/x0xx00000x

Peichao Zou[1, #], Chunyang Wang[1, #], Yubin He[1], Huolin. L. Xin[1]*

A challenging task in solid-state batteries is finding a solid ionic conductor that simultaneously is electronically insulative, stable at both low and high voltages, and sustainable. Current prevalent ceramic lithium-ion conductors (LICs) struggle to balance all the criteria, and their selection is limited for application in solid-state lithium metal batteries. Here, we report a universal solid electrolyte design paradigm, i.e., inorganic LIC sandwiched between solid electronic separators, to allow a broad range of inorganic LICs including $Li_{1.5}Al_{0.5}Ti_{1.5}(PO_4)_3$, LiV_3O_8, and $Li_4Ti_5O_{12}$, to be deployed in solid-state lithium batteries. With the solid electrolyte design, the requirements of electronic insulation or (electro)chemical stability for ceramic LICs are no longer needed. A high critical current density of 14 mA cm^{-2} (under a constant plating/stripping capacity of 0.5 mAh cm^{-2}) and long-life cycling (7,000 hours at 0.2 mA cm^{-2} and 2,500 hours at 0.5 mA cm^{-2}) were realized in Li//Li symmetric cells at room temperature. Remarkably high capacity retentions (87% after 400 cycles) were also achieved in Li^0 full cells paired with $LiNi_{0.8}Mn_{0.1}Co_{0.1}O_2$ cathodes (mass loading: 7.4 mg cm^{-2}). Our discoveries promise the implication of broader-ranging, more sustainable, yet previously unrecognized ionic conductors in practical solid-state batteries.

Broader context

In the past half a century, a host of solid ionic materials, i.e., garnets, (anti)perovskites, halides, sulfides, NASICONs, were discovered for conducting lithium ions. Most of them are unstable towards lithium metal anodes. The rare materials that have a cathodic stability window down to 0 V (vs. Li/Li^+) are garnet materials, which yet contain lanthanum (La), a rare earth element and critical material. We know that there are a handful of battery anode materials that are reasonable Li-ion conductors, constitute only earth-abundant materials, and can be discharged to 0 V (vs. Li/Li^+) without large volume expansion and phase conversion. However, there are rare reports using these electrode materials as solid electrolytes, because these materials typically have electronic conductivities that are orders of magnitude higher than that required for solid electrolytes. Here, we leverage a simple sandwich-type solid electrolyte architecture design to enable any ceramic lithium-ion conductors to be deployed in solid-state batteries, and the requirements of electronic insulation or (electro)chemical stability for the ceramic lithium-ion conductors are no longer needed. With our solid electrolyte design, a broad range of ionic conductors, including lithium battery electrode materials, has been applied in solid-state lithium metal batteries with superior cycle life.

Introduction

Lithium metal (Li^0), with a specific capacity of 3860 mAh g^{-1} and a volumetric capacity of 2061 mAh cm^{-3}, has been hailed as a promising anode material for next-generation lithium batteries. The implementation of Li metal anode can boost both the gravimetric and volumetric energy density of lithium metal batteries (LMBs) compared with state-of-the-art lithium-ion batteries (LIBs).[1-3] When further coupling the Li^0 anode with a non-flammable solid-state electrolyte (SSE), the safety level of LMBs can be substantially improved.[3, 4] Current SSEs can be generally divided into inorganic SSEs, polymeric SSEs, and their combination. Compared with polymeric SSEs, inorganic SSEs can deliver higher ionic conductivity, better thermal stability, and higher mechanical strength.[3, 5, 6]

Traditionally, a solid electrolyte for LMBs shall satisfy the following four criteria:[6-8] 1) it should conduct Li ions; 2) it should be a wide-band-gap electronic insulator; 3) it shall not react with Li continuously; 4) it should have anodic stability to pair with high-voltage cathodes. Thus far, a considerable number of lithium-ion conductors (LICs) have been discovered and explored as potential inorganic SSEs, including lithium phosphorous oxynitride, sodium superionic conductor (NASICON)-, (anti)perovskite-, garnet-, halide-, and sulfide-type LICs.[5, 7, 9, 10] In practical, however, most inorganic LICs can hardly meet criteria 2), 3), 4) simultaneously and are particularly unstable against Li metal.[11] For instance, aluminum- and titanium-rich $Li_{1+x}Al_xTi_{2-x}(PO_4)_3$ is thermodynamically stable up to ~4.3 V (vs. Li^+/Li), yet they are easily reduced below 2 V (vs. Li^+/Li);[11] transition metal-free sulfide SSEs such as Li_6PS_5Cl exhibit a much narrow ESW (1.1~2.8 V).[12] The high "reactivity" of these inorganic SSEs toward low-voltage lithium reduction and/or high-voltage oxidation leads to undesired decomposition interphase formation at both the anode-SSE interface and the cathode-SSE interface (**Figure 1**a). The rare ceramic solid electrolyte material that is relatively

[1]*Department of Physics and Astronomy, University of California, Irvine, California 92697, United States*
[#]*These authors contributed equally to this work.*
**Correspondence: huolinx@uci.edu*

stable against Li^0 anodes is garnet-type materials,[7, 11] i.e., $Li_7La_3Zr_2O_{12}$ (LLZO) and $Li_{7-x}La_3Zr_{2-x}Ta_xO_{12}$ (LLZTO); yet, their wide application poses a sustainability challenge to the whole emerging solid-state battery industry since lanthanum (La) is a rare earth element and critical material.

Aside from the traditional LICs mentioned above, there are a handful of LIB electrode materials that are reasonable earth-abundant Li-ion conductors, with ionic conductivity at ~0.1 mS/cm level or higher at room temperature (r.t.). However, there are rare reports using these electrode materials as solid electrolytes. The reason is that a solid-state electrolyte has to be a good electronic insulator (criteria 2), while LIB electrode materials typically have electronic conductivities that are orders of magnitude higher than that required for solid electrolytes. They are classified as mixed ionic electronic conductors (MIECs). Even MIECs are 0 V-stable, the high electronic conductivity in bulk and/or at the grain boundary of MIECs will promote dendritic/dead Li formation within the SSE and/or at the cathode-SSE interface, finally short-circuiting the cell (Figure 1b). Therefore, it is of both scientific and industrial importance to overcome the criteria 2), 3), 4) for ceramic ionic conductors. Relevant breakthrough would broaden the LIC selection and allow us to build solid-state LMBs in a more economical and sustainable way.

In the past decade, SSE architecture designs, such as multi-layered SSE and composite SSE designs, have become an effective approach to resolve the interfacial decomposition issue of traditional inorganic LICs for LMBs.[13-17] Yet, leveraging such a strategy to extend the application of LIB electrode materials as LICs for solid-state batteries remains unexplored. In this work, we report a proof-of-concept SSE architecture design strategy to broaden the selection of solid electrolyte materials for sustainability and battery practicality. Within our SSE architecture (Figure 1c), electronically conductive ceramic materials or even materials that react with Li metal and/or are unstable at high voltages, become compatible with solid-state LMBs. This is realized by sandwiching inorganic LICs/MIECs between two "solid electronic separators", i.e., UV-polymerized poly-acrylate (UVEA) films, that are perfectly electronic insulating (6.65×10^{-9} S/cm at r.t.), ionic-conductive (7.73×10^{-4} S/cm at r.t.), and stable against Li^0 reduction and high-voltage oxidation (ESW: 0-4.6 V vs. Li^+/Li). The solid electronic separator prevents any electrochemical reaction

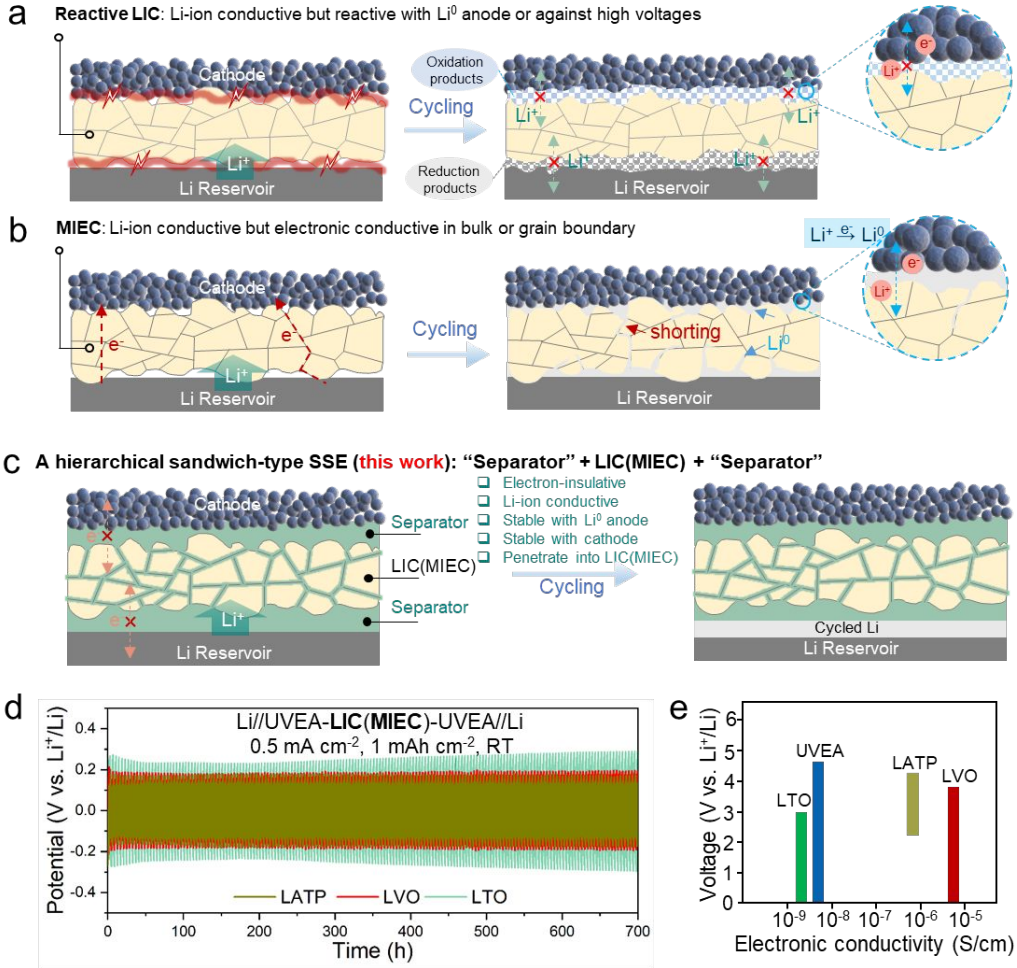

Figure 1. Schematic and electrochemical performance of sandwich SSE. Schematic of anode/cathode-SSE interphase evolution in solid-state batteries when using traditional undesired SSE: (a) Li-ion conductors that are reactive with Li^0 anode or cathode and (b) mixed Li-ion and electron conductors. (c) Schematic of anode/cathode-SSE interphase evolution in solid-state batteries when using a sandwich-type SSE proposed in this work. (d) Discharge/charge profiles of solid-state Li//Li symmetric cells showing the feasibility of both reactive LIC and MIEC for SSE when adopting a sandwich configuration. The cycling current density was 0.5 mA cm^{-2}, and the cycling capacity was 1 mAh cm^{-2}. (e)

Electrochemical stability window (without decomposition) and electronic conductivity of adopted LICs demonstrated in this work. Note that the 0V- stability of LTO has been reported by our previous work[18], while the 0V-stability of LVO was proved by our preliminary results that delivers a similar working mechanism to that of another reported V-based oxide[19].

between electrodes and ceramic LICs, and its penetration into the inorganic LIC/MIEC guarantees sufficient ionic conductivity of the whole sandwich SSE. Using UVEA—a polymeric LIC—as a model system, we systematically demonstrated the practicality of three sustainable ceramic LICs for solid-state LMBs, including both typical inorganic LICs ($Li_{1.5}Al_{0.5}Ti_{1.5}(PO_4)_3$, LATP) and unpopular inorganic LICs (LiV_3O_8 (LVO) and $Li_4Ti_5O_{12}$ (LTO); note these two LICs are traditional LIB electrode materials) for the first time. Stable cycling (over 700 hours) with high Li^0 reversibility of sandwich SSEs have been demonstrated in Li//Li systematic cells, regardless of the electronic conductivity and ESW of as-adopted inorganic LICs/MIECs (Figure 1d, e). More interestingly, sandwich SSEs-based Li^0//$LiNi_{0.8}Mn_{0.1}Co_{0.1}O_2$ full cells exhibited excellent cycling stability at room temperature (22 ^oC), which also presented a negligible discharge capacity decay in the low N/P ratio condition. The generality and superior electrochemical performance of sandwich SSEs were attributed to the mitigated parasitic SSE decomposition, robust SEI layer formation, and dense Li metal evolution morphology, as jointly revealed by Cryo-electron microscopy and X-ray photoelectron spectroscopy characterization.

Results and discussion

Design and characterization of sandwich SSE

In principle, to be a good solid electronic separator, it should ideally satisfy the afore-mentioned four criteria. In this study, the polymeric UVEA film based on succinonitrile (a classic molecular plastic crystal) was designed as a model system, which was prepared by a one-step solvent-free UV-polymerization approach.[20, 21] Specifically, the UVEA is composed of lithium bis (trifluoromethanesulfonyl) imide (LiTFSI, lithium salt), ethylene acrylate (EA, monomer), ethylene glycol dimethyl acrylate (EDA, cross-linker to improve the mechanical properties), succinonitrile (SN, solid crystal plasticizer to improve the conductivity),[22] and fluoroethylene carbonate (FEC, SEI-forming additive for stabilizing lithium metal anodes),[23, 24] which was first casted onto a reinforcement and then subject to UV irradiation for 10 minutes (see method). Note that the thickness of UVEA film can be simply adjusted by changing the reinforcement with different thicknesses (Figure S1). UVEA films based on a glass fiber membrane were primarily fabricated to validate the hypothesis in this work, unless noted otherwise. According to the liquid-state ^1H nuclear magnetic resonance (NMR) measurement, no residual monomers/oligomers could be detected in UVEA after polymerization (Figure S2), indicating that the monomer conversion yield was 100%. TG-DSC-MS test further indicates that EA and EDA have been completely polymerized, and there is no free FEC additive in UVEA (Figure S3). Combining the fact that SN (plasticizer) is solid at room temperature, the UVEA film is considered solid at room temperature. The solid nature of UVEA polymer is further confirmed by the high storage modulus of ~100 MPa and low loss modulus in the range of 10–30 MPa, as measured by the dynamic mechanical analysis (Figure S4a).

Electrochemical test suggests that the obtained UVEA layer could deliver a high room-temperature ionic conductivity of 7.73×10^{-4} S/cm, an low electronic conductivity of 6.65×10^{-9} S/cm, a wide electrochemical stability window of 0-4.6 V (vs. Li^+/Li), and a relatively high Li^+ transference number of 0.51, as shown in Figure S5. Beneficial from the high ionic conductivity and good interfacial contact, UVEA renders a low dynamic current resistance of around 350 ohms in a symmetric Li//Li cell configuration (Figure S6 and Table S1). In addition, the UVEA film exhibits a good tensile strength of 1.1 MPa and reasonable elastic modulus of 100 MPa (Figure S4). Owing to the highly crosslinked polyacrylate backbone, its restricted chain mobility, and lower solvating ability towards Li^+, an Arrhenius-type ion conduction mechanism[25] was realized in UVEA, consistent with the temperature-dependent conductivity curve (a linear relationship between log σ and 1000/T, Figure S7). These properties make UVEA ideally qualified as the solid electronic separator that allows fast ionic conduction but block the electron transport between inorganic LICs and anodes/cathodes. Note that although the above-mentioned physicochemical properties of UVEA make it a seemingly promising polymer electrolyte, UVEA film exhibits poor ability in prohibiting dendrite growth and penetration due to its insufficient mechanical strength, particularly at high current densities and/or high cycling capacities (will be discussed later). Therefore, it is essential to combine UVEA with inorganic LICs to enhance the cell's lifetime and reduce the safety risk.

The fabrication of inorganic LICs (LATP, LVO and LTO) was realized through a cold-pressing protocol with/without high-temperature annealing, depending on the types of LICs (see experimental section). Thereafter, the sandwich SSEs were achieved by physically stacking the UVEA film, one inorganic LIC layer, and the UVEA film together. According to the electrochemical impedance spectroscopy (EIS) test, the ionic conductivity of pure LATP, LVO, and LTO pellets was measured to be 3.58×10^{-5} S/cm, 3.18×10^{-5} S/cm, and 2.97×10^{-6} S/cm, respectively (Figure S8). Despite the relatively low intrinsic ionic conductivity of ceramic pellets, the contact resistance at UVEA/ceramics and UVEA/Li as well as the charge transfer resistance in sandwich SSEs can be dramatically lowered (Figure S9a, b), rendering an overall ionic conductivity of 0.4-0.7 mS/cm for sandwiched SSEs based on LATP, LVO, and LTO (Figure S9c and summarized in Table S2). This is owing to the softness of the polymeric UVEA, which not only enables an intimate contact between UVEA and ceramics/Li (Figure S10) that reduces the interfacial resistance, but also slightly infiltrates into ceramics (particularly when ceramics are porous) that provides additional ionic transfer pathway inside the ceramics (Figure S11-13). The similar-magnitude overall resistance of different sandwich SSEs also explains the comparable overpotential in symmetric Li//Li cells (Figure 1d) and comparable capacity in full cells when using different sandwich SSEs (will be discussed later in Figure 4e).

In general, a higher ionic conductivity of inorganic LICs will lead to lower battery overpotentials, as demonstrated by the smaller overpotential of UVEA-LATP-UVEA-based cell over those using LTO and LVO-based SSEs (Figure 1d). The necessity of ionic conductivity of inorganic layers for the sandwich SSE design is further confirmed by the huge overpotential when using an inert SiO_2 layer (Figure S14a).

Li^0 reversibility and morphology evolution with MIEC-based sandwich SSE

A challenging issue for mixed ionic-electronic conductors as SSEs of solid-state LMBs is the uncontrolled Li metal plating within the SSE and even on the SSE-cathode interface, as discussed above in Figure 1b. To validate the capability of solid electronic separator (UVEA film in this work) in prohibiting the electronic shuttling and Li^0 penetration, we conducted the Li plating experiment in an Li//Cu asymmetric cell using UVEA-MIEC and UVEA-MIEC-UVEA as the SSE. The asymmetric cell setup is illustrated in **Figure 2**a, b. Without the solid electronic separator between Cu foil and MIEC (LVO here for demonstration, which has a relatively high electronic conductivity of 7.98×10^{-6} S/cm as shown in Figure S15a and has previously used as LIB cathode materials[26-29]), dendritic and loose Li deposits were identified directly on the top surface of lithiated MIEC pellet (Figure 2b, c). In comparison, after introducing UVEA film as the solid electronic separator between MIEC layer and Cu foil, a smooth and dense Li^0 morphology on the Cu foil surface (Figure 2e) without Li deposition on the MIEC surface (Figure 2f) was observed. These results reveal the feasibility of MIECs as SSE once their surface is electronically insulated.

Cryo-TEM imaging was further employed to understand the morphology and structure of Li^0 deposits using the UVEA-LVO-UVEA sandwich electrolyte. Consistent with the SEM morphology (Figure 2d), the low-magnification Cryo-TEM image showed that the Li^0 deposits were densely packed and had a flat chunk morphology (Figure 2g). High-magnification Cryo-TEM image in Figure 2h showed that, similar to the case in the UVEA-LATP-UVEA system (Figure 3h, I, will be discussed later), a thin and uniform layer of SEI was formed

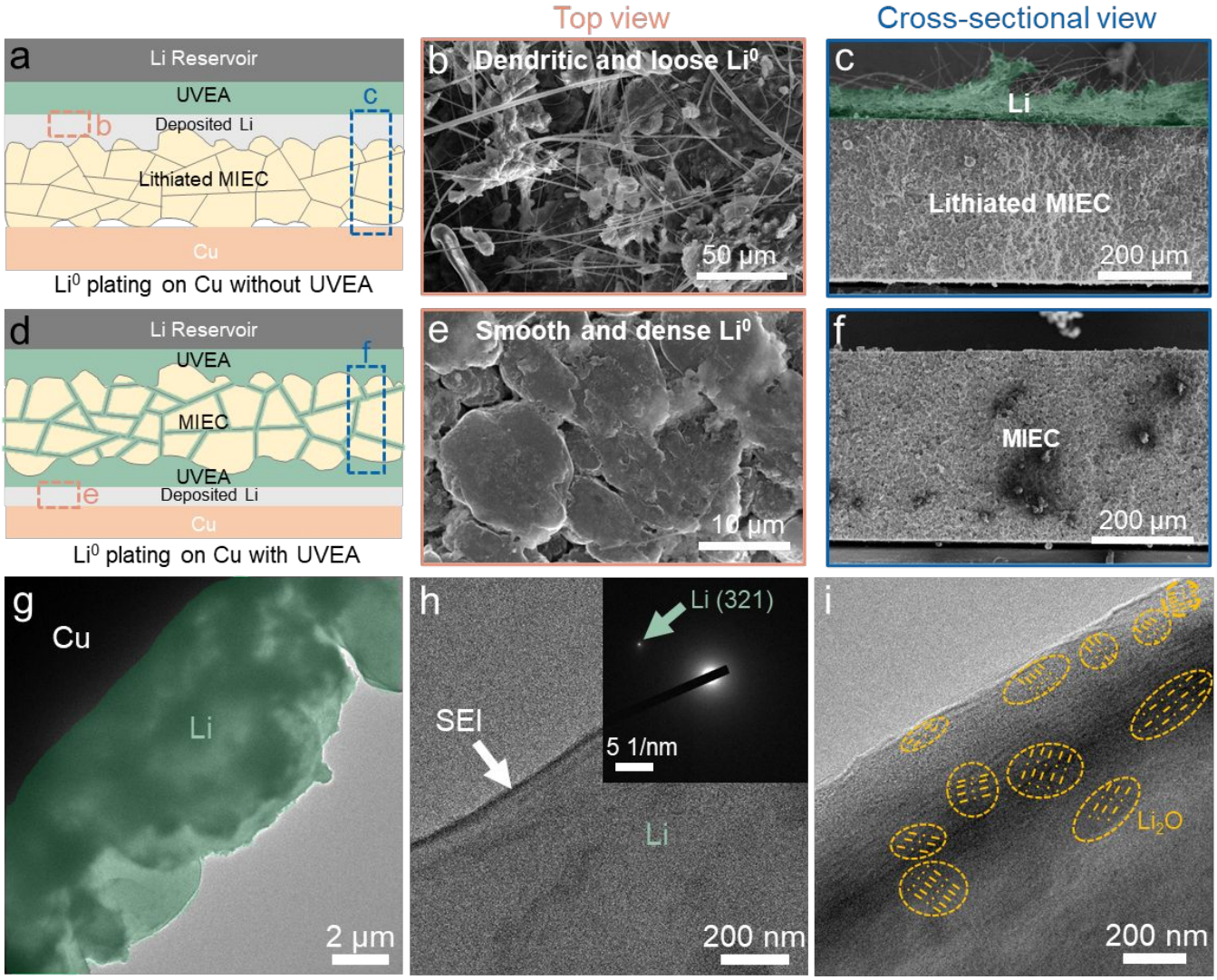

Figure 2. Morphology and solid-electrolyte interphase investigation of plated Li metal in UVEA-LVO-UVEA electrolyte. Schematic setup of Li//UVEA-MIEC//Cu cell (a) and Li//UVEA-MIEC-UVEA//Cu cell (d). (b, c) SEM images of MIEC (LVO) pellet extracted from Li//UVEA- MIEC//Cu cell: (b) top view and (c) cross-sectional view. (e) Top view SEM image of plated Li^0 on Cu using the Li//UVEA-MIEC-UVEA//Cu cell. (f) cross-sectional SEM image of MIEC (LVO) pellet extracted from Li//UVEA-MIEC-UVEA//Cu cell. The Li plating experiment was conducted at a current density of 0.2 mA cm^{-2}. (g) A representative low-magnification Cryo-TEM image showing the morphology of the Li^0 deposits on Cu grid using the UVEA-LVO-UVEA sandwich electrolyte. (h) A representative high-magnification Cryo-TEM image and corresponding EDP of a Li^0 deposit. Note that the signal from the SEI is not effectively detected in the EDP because the SEI is much smaller in proportion to the thick Li^0. (i) Atomic-

resolution Cryo-TEM image of the deposited Li^0 with an SEI composed of nanocrystalline domains (e.g., Li_2O indicated by dash circles) with random crystallographic orientations.

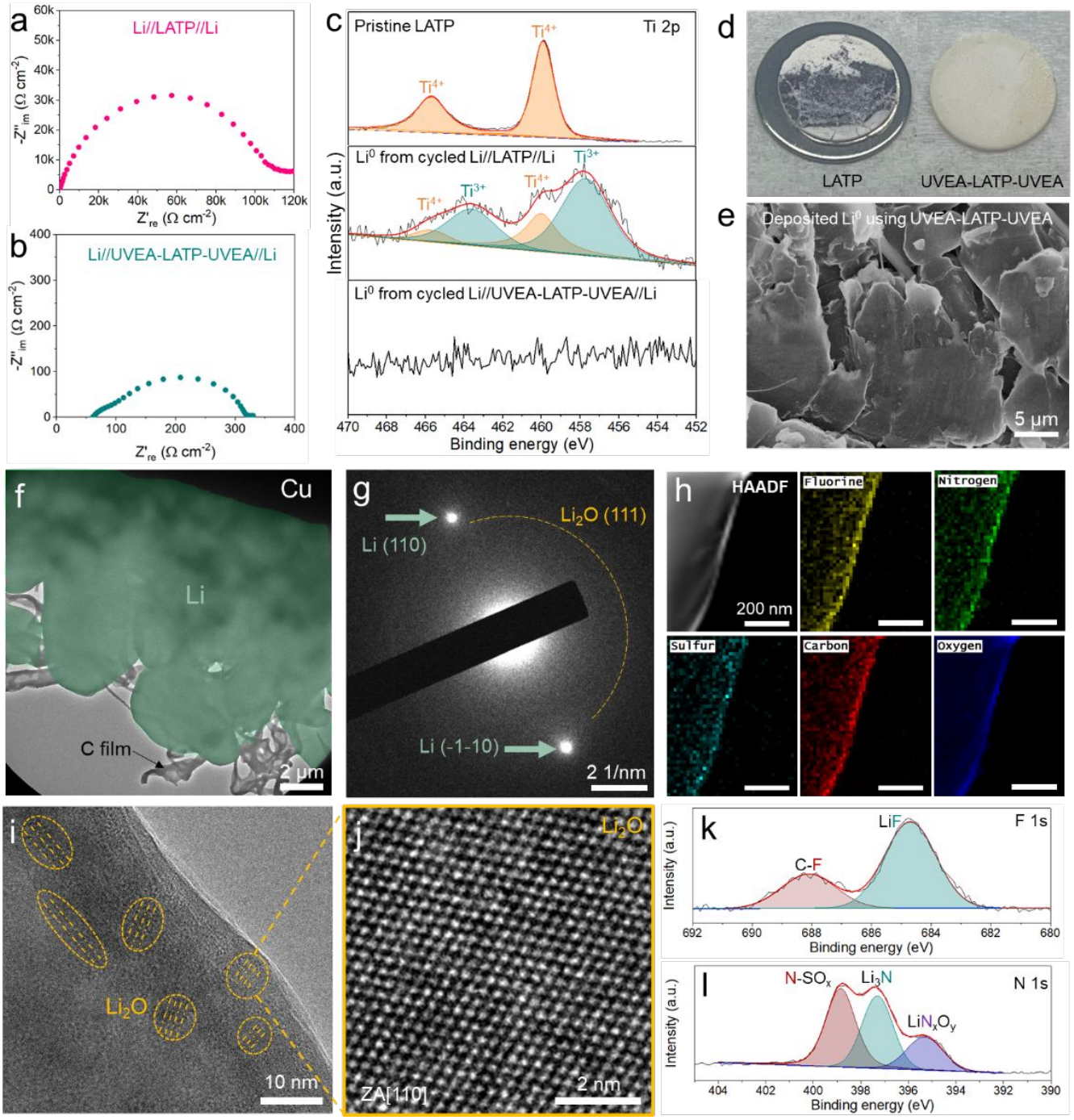

Figure 3. Interfacial resistance, morphology, and solid-electrolyte interphase investigation of plated Li metal in UVEA-LATP-UVEA electrolyte. EIS of (a) Li//LATP//Li and (b) Li//UVEA-LATP-UVEA//Li symmetric cells at pristine state. (c) Ti 2p XPS spectra of (top) pristine LATP powder, (middle) Li^0 from cycled Li//LATP//Li, and (bottom) Li^0 from cycled Li//UVEA-LATP-UVEA//Li. (d) Digital images of LATP pellets from cycled (left) Li//LATP//Li and (right) Li//UVEA-LATP-UVEA//Li. (e) SEM image of deposited Li^0 on Cu foil surface. (f) Cryogenic transmission electron microscopy (Cryo-TEM) image showing the morphology of the deposited Li^0 using the UVEA-LATP-UVEA sandwich electrolyte. (g) Electron diffraction pattern (EDP) corresponding to the Li^0 deposit in (f). Bragg spots corresponding to Li^0 and a weak diffraction ring corresponding to Li_2O are indicated by the arrows and the dash line, respectively. (h) High-angle annular dark-field scanning transmission electron microscopy (HAADF-STEM) image and energy-dispersive spectroscopic (EDS) maps of the deposited Li^0 using the UVEA-LATP-UVEA sandwich electrolyte. The result shows that a thin layer of solid electrolyte interface (SEI) enriched in C, N, O, F, S forms on the Li^0 surface. (i)

Atomic-resolution Cryo-TEM image of the Li^0 deposit and (j) highlight of a Li_2O nanocrystal in the SEI. (k) F 1s and (l) N 1s XPS spectra of Li^0 from cycled Li//UVEA-LATP-UVEA//Li.

on the surface of the Li^0 deposit. Figure 2i shows a representative atomic-resolution Cryo-TEM image of the Li^0 deposit. The SEI derived from the UVEA-LVO-UVEA electrolyte was composed of nanocrystalline domains with random crystallographic orientation (e.g., Li_2O crystals indicated by the dash circles in Figure 2h).

Traditionally, using phases with significant electronic conductivity in SSE will improve the short-circuit risk, as any electronic leak in the SSE (e.g., a dendrite reaching from the Li anode through the polymer protective layer to the electronic-conductive LIC) will render it easier for Li^+ to receive electrons and directly generate Li dendrites within the SSEs. Therefore, a higher electronic conductivity for the inorganic LICs will make it easier to trigger the cell short-circuit. Nevertheless, the cell short-circuit risk will be greatly reduced using our SSE designs even if highly electronic-conductive LICs are deployed. This is because there are two polymeric layers that can double-block the electronic leakage. If lithium dendrites (from the anode side) penetrate one polymer layer, the other polymer layer (between SSE and cathode) would play as the second defence line to protect the cell from shorting. More importantly, the two LICs of choice in this work (LTO and LVO, at the pristine state, namely at 0% state of charge) can react with penetrated Li through the lithiation of LTO and LVO, thus consuming penetrated Li, suppressing its further penetration, and minimizing the short-circuit risk. Such a unique property has rarely been reported in traditional composite polymer electrolytes (CPE), where inorganic particles are primarily used to reinforce the mechanical properties of CPE.

Aside from LVO, we also selected $LiNi_{0.8}Co_{0.1}Mn_{0.1}O_2$ as another MIEC, which has both high ionic conductivity (4.1×10^{-3} S/cm at 20 °C) and electronic conductivity (4.1×10^{-3} S/cm at 20 °C).[30] As shown in Figure S16, the symmetric Li//Li cell based on UVEA-NMC811-UVEA can stably cycle for 800 hours without shorting at the cycling current density of 0.5 mA cm^{-2}. This strongly confirms that our proposed sandwich SSE design can effectively block the electronic shuttling and enable the implication of MIECs.

Interfacial stability of reactive LIC-based sandwich SSE against reduction

The generality of sandwich-type SSE was also examined using LATP as the inorganic LIC component, since LATP is a popular and representative LIC that is unstable against Li reduction.[11, 31] **Figure 3**a, b shows the impedance result of fresh Li//Li symmetric cells (resting 2 hours) using the bare LATP and sandwich UVEA-LATP-UVEA as the SSE. It indicated that bare LATP-based cell presented huge interfacial resistance at the magnitude of 10^5 ohm cm^{-2}, while the UVEA-LATP-UVEA-based cell delivered much lower interfacial resistance and charge-transfer resistance. This is strong evidence that UVEA film can effectively protect LATP from reduction reaction, which was further supported by the XPS analysis. As shown in Figure 3c, the Ti 2p XPS spectra revealed that cycled Li^0 electrode from Li//UVEA-LATP-UVEA//Li showed no apparent Ti signal. In contrast, the Ti signal on the Li^0 electrode can be well recognized when cycling using bare LATP, and the Ti signal can be further deconvoluted into Ti^{3+} and Ti^{4+}. The appearance of Ti^{3+} signal correlated well with the LATP reduction.[32-34] The protection of UVEA film was also validated by the color change of LATP pellets with/without UVEA film after cycling in symmetric Li//Li cells (Figure 3d), where bare LATP turned into black while UVEA-wrapped LATP maintained the original light yellow color.

Scanning electron microscopy (SEM) characterization manifested that the plated Li^0 on Cu foil presented a smooth Li chunk morphology when using the UVEA-LATP-UVEA sandwich electrolyte, which is partially attributed to the existence of inorganic LATP that enhances the mechanical strength of sandwich SSE and helps to suppress the dendritic Li formation. Cryogenic transmission electron microscopy (Cryo-TEM) imaging and spectroscopic analysis were further employed to understand the morphology and structure of the Li^0 deposits using the sandwich electrolyte. Figure 3f and Figure S17, 18 are representative Cryo-TEM images showing the morphology of the deposited Li^0. In good agreement with the SEM morphology, the Cryo-TEM results suggested that the Li^0 deposits on Cu were densely packed and had a smooth chunk morphology. Figure 3g shows a representative electron diffraction pattern (EDP) corresponding to the Li^0 deposit in Figure 3f. A pair of strong Bragg spots (indicated by arrows) corresponding to the (110) planes of Li^0 as well as a weak diffraction ring (indicated by a dash line) corresponding to Li_2O were identified. Energy-dispersive spectroscopic (EDS) maps (Figure 3h) corresponding the region in the high-angle annular dark-field scanning transmission electron microscopy (HAADF-STEM) image showed that a thin layer of solid electrolyte interface (SEI) enriched in C, N, O, F, S formed on the surface of the Li^0 deposit. Figure 3i, j show atomic-resolution Cryo-TEM images of the Li^0 deposit. It is seen that the SEI is composed of nanocrystalline domains with random crystallographic orientation (e.g., Li_2O crystals indicated by the dash lines in Figure 3i) and the atomic structure of a Li_2O nanocrystal is highlighted in Figure 3j.

XPS further confirmed the enrichment of F- and N-containing components in the UVEA-derived SEI formed on the Li^0 anode surface. The F1s spectra show a distinct peak at around 684.8 eV (Figure 3k), which can be assigned to LiF. Here, LiF as the reduction product of FEC additive in UVEA has been reported to promote the formation of a compact and stable SEI layer.[23, 35] The N1s profile in Figure 3l suggests the existence of Li_3N in the SEI layer, which has also been recognized as a favorable inorganic SEI component due to its high lithium-ion conductivity. Both Cryo-TEM and XPS characterization prove that the UVEA polymer layer will contribute to a stable SEI layer, which is favorable to improve the interfacial stability and Li^0 reversibility.

Electrochemical performance of sandwich-type SSEs

The significant advantages of inorganic LIC-based sandwich SSEs in blocking the dendritic Li^0 penetration was exemplified by the high critical current density (CCD) at room temperature for both reactive LIC-based sandwich SSE (>14 mA cm^{-2} for UVEA-LATP-UVEA, **Figure 4**a) and MIECs-based sandwich SSE (9 mA cm^{-2} for UVEA-LVO-UVEA, Figure S19) when tested at a constant capacity of 0.5 mA cm^{-2} or a

constant plating/stripping time of 0.5h (> 5 mA cm^{-2} for both UVEA-LATP-UVEA and UVEA-LVO-UVEA, Figure S20). Notably, the high CCD achieved in this work is far sufficient to meet the practical operation current density demand for commercial cells (3 mA cm^{-2}, corresponding to 1C charge/discharge rate for a cell with an areal capacity of 3 mAh cm^{-2}), which also outperforms most of recently reported CCD results[36] for both inorganic SSE and polymeric SSE, or their combination (Table S3).

One challenge of solid-state LMBs is the poor Li^0 reversibility, which is originated from the poor interfacial contact Li-SSE, the SSE decomposition, void/pore accumulation on Li metal surface and further dendritic/dead Li formation. In this study, Li//Li symmetric cells using our proposed sandwich SSEs, including LTO-, LVO-, and LATP-based ones, can be initiated and stably operated at room temperature for more than 700 hours at 0.5 mA cm^{-2} with a Li^0 plating/stripping capacity of 1 mAh cm^{-2} (Figure 1d and Figure S18), suggesting the excellent Li^0 reversibility enabled by the intimate Li-SSE contact, favorable UVEA-derived SEI layer, and dense-packed Li morphology. In sharp contrast, Li//Li symmetric cells using the bare inorganic LIC/MIEC baselines can either hardly be initiated or show a short cycle life (Figure S21). For example, Li//LATP//Li cell showed a fast overpotential ramping up to 4 V within 4 hours even cycling at a much low current density of 0.05 mA cm^{-2} (Figure S21a). This is mainly due to the parasitic reduction reaction of LATP by Li metal, which leads to unwanted decomposition product accumulation and speeds up the Li-SSE interface failure. More interestingly, a much longer lifetime has been realized for Li//UVEA-LATP-UVEA//Li symmetric cells, e.g., 2500 hours at 0.5 mA cm^{-2} (Figure 4b), 7000 hours at both 0.05 mA cm^{-2} and 0.1 mA cm^{-2} (Figure S22a, b), and 300 hours at a higher current density of 1 mA cm^{-2} with a higher cycling capacity of 2 mAh cm^{-2} (Figure S22c). When directly using the UVEA layer as the SSE, the symmetric Li//Li cell can only operate for 520 hours at 0.5 mA cm^{-2} (Figure 4b) and was shorted after only 50 hours at 1 mA cm^{-2} (Figure S22c). This is because UVEA is too soft to inhabit dendritic growth and penetration alone.

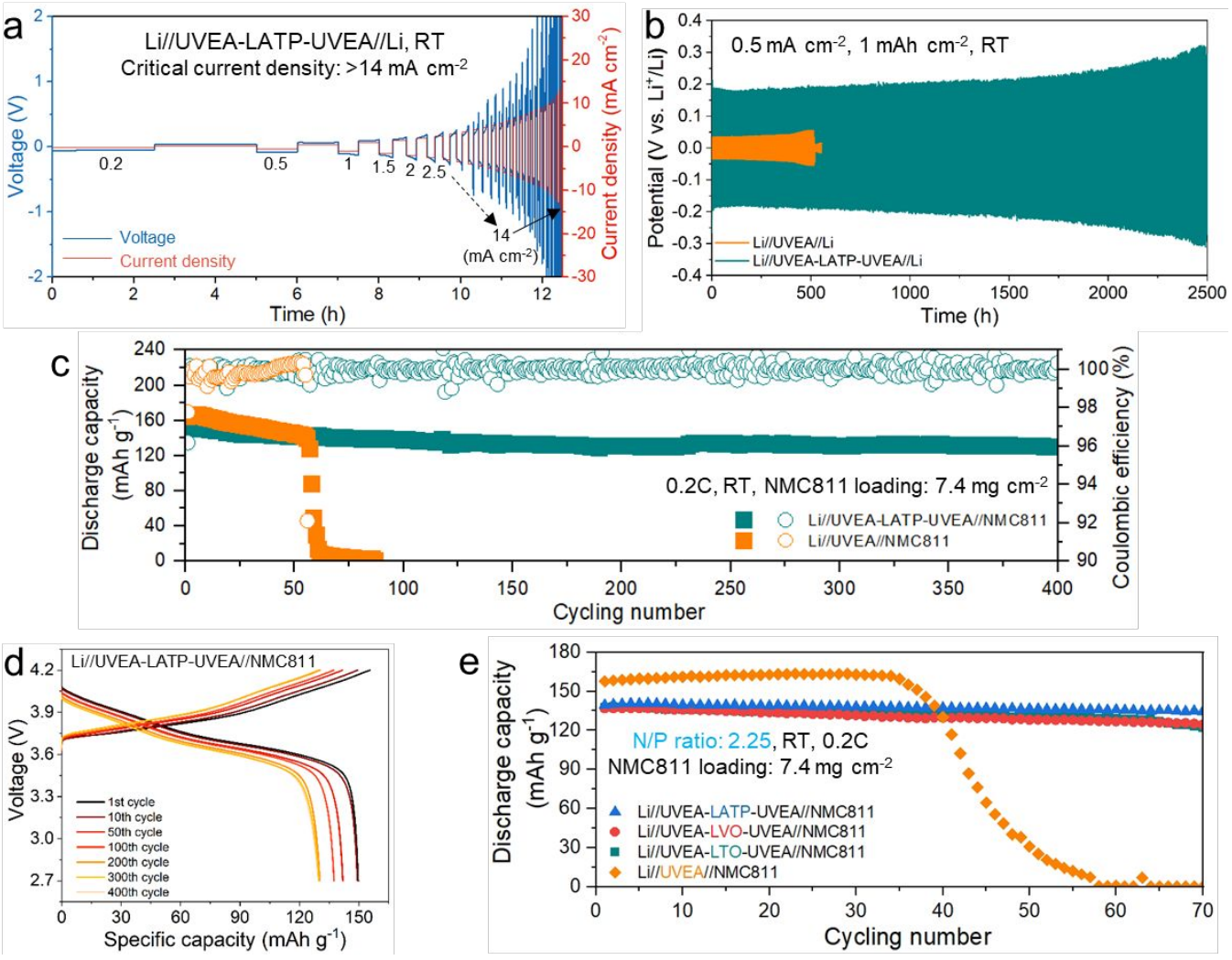

Figure 4. Electrochemical properties of sandwich SSEs. (a) Critical current density of UVEA-LATP-UVEA tested in symmetric Li//Li cells at 22 °C (RT). The Li//Li symmetric cell was cycled under step-up current densities with a constant plating/stripping capacity of 0.5 mAh cm^{-2}, and no short circuit occurred before 14 mA cm^{-2}. (b) Discharge/charge profile of solid-state Li//UVEA-LATP-UVEA//Li and Li//UVEA//Li battery at a current density of 0.5 mA cm^{-2} and a cycling capacity of 1 mAh cm^{-2}. (c) Cycling stability of Li//UVEA-LATP-UVEA//NMC811 and Li//UVEA//NMC811 cells at 0.2 C. (d) corresponding charge/discharge profiles of Li//UVEA-LATP-UVEA//NMC811 cells at 0.2 C. The areal mass

loading of NMC811 in (c, d) is ~7.4 mg cm^{-2}. (e) Cycling performance of bare UVEA and sandwich-type SSEs based solid-state cells with NMC811 cathodes under a theoretical N/P ratio of 2.25. The cells were cycled at 0.2 C and RT (22 °C) with 2 mAh cm^{-2} of Li^0 (deposited on Cu foil) as the anode.

To validate the feasibility of sandwich-type SSEs in full cells, we constructed solid-state LMBs using $LiNi_{0.8}Mn_{0.1}Co_{0.1}O_2$ (NMC811) cathode with a mass loading of ~7.4 mg cm^{-2} (without catholyte) and excess Li^0 as the anode. As shown in Figure 4c, the Li//UVEA-LATP-UVEA//NMC811 full cell delivered a capacity retention of 87% at 0.2C and RT after 400 cycles (voltage range: 2.0-4.2 V, ~2400 hours). In addition, the low voltage fading upon cycling (Figure 4d) is indicative of excellent interfacial stability between sandwich SSEs with both NMC811 cathode and Li^0 anode. Similarly, Li//NMC811 full cell using LVO-based sandwich SSE can also stably run for 300 cycles with a low capacity decay (Figure S23). Owing the wide electrochemical stability window of UVEA film (0-4.6 V), solid-state Li//NMC811 showed stable cycling even when tested at a higher charge cut-off voltage of 4.4V (Figure S24). To further evaluate the feasibility of sandwich SSEs in practical cells, we assembled low N/P ratio solid-state Li//NMC811 full cells by leveraging 2 mAh cm^{-2} of Li^0 as the anode (deposited on Cu foil in liquid electrolyte, see experimental). Coupling with the NMC cathodes (7.4 mg cm^{-2}, corresponding to an estimated areal capacity of around 1.6 mAh cm^{-2}), the N/P ratio was theoretically lowered to 2.25 (see method). Under this harsh condition, regardless of using LTO, LVO or LATP as the inorganic LIC in sandwich SSEs, the full cell's capacity almost overlapped and only slightly dropped from around 137 mAh g^{-1} to around 125 mAh g^{-1} after 70 cycles (Figure 4e), exhibiting a capacity retention of 91%. These results strongly validate the versatility and superiority of our proposed sandwich SSEs for the application of solid-state lithium metal batteries.

Discussion and conclusions

For real battery applications, the thickness of SSE shall be as small as possible. Under this context, we propose to further reduce the thickness of solid separator (UVEA here) by directly coating the UVEA film onto the surface of ceramic pellets via the dip-coating (or spin-coating) and subsequent UV polymerization processes, with which the thickness of surface UVEA layer can be decreased to even around 1 μm (Figure S25). In addition, considering the poor processibility issue of ceramic LIC pellets, a composite SSE architecture, i.e., uniformly dispersing ceramic LIC fillers within polymeric UVEA matrix, was also propose. Such SSE architecture designs can not only broaden the solid electrolyte materials selection, but also render more functionalities in delaying the dendrite-induced short circuit and extending the cell's cycle time. For demonstration, $Li_{1.5}Al_{0.5}Ti_{1.5}(PO_4)_3$, LiV_3O_8, and $Li_4Ti_5O_{12}$ were also selected as the filling materials, which are the same as those used in the sandwich SSE architecture. The electrochemical test shows that all composite SSEs exhibit longer cycling lifetime in symmetric Li//Li cells than neat UVEA film, as shown in Figure S26. If ceramic LICs can be electrochemically lithiated or are chemically reactive towards Li metal, the ceramic fillers would be capable of consuming irregular Li protrusions/dendrites once they are physically contacted.

In summary, we report a solid-state electrolyte configuration that effectively broadens the inorganic ionic conductor selection for batteries. The key design principle is to protect inorganic ionic conductors with ionic-conductive but electronic-insulative solid separators. We have thoroughly demonstrated the feasibility of three highly distinct Li-ion conductors (varying from conventional solid electrolyte to electrode active materials) in all-solid-state lithium-metal full cells with superior cyclability and low N/P ratio. This work offers a drop-in solution for applying conventional reactive and electronic-conductive inorganic lithium-ion conductors in solid-state lithium batteries. The SSE architecture design strategy broadens the SSE selection and design, holding great potential in lowering SSEs' cost and further improving their sustainability.

Author contributions

H.L.X. conceived the idea. P.Z. and C.W. contributed equally to this work. All authors designed the experiments. P.Z. and Y.H. prepared the materials and performed the electrochemical experiments. C.W. performed the TEM experiments. All authors contributed to the discussion of content, and writing and editing of the article prior to submission.

Conflicts of interest

There are no conflicts to declare.

Acknowledgements

This work was supported by the U.S. Department of Energy under contract no. DE-SC0021204 and the startup funding of H.L.X. The authors acknowledge the use of facilities and instrumentation at the UC Irvine Materials Research Institute (IMRI), which is supported in part by the National Science Foundation through the UC Irvine Materials Research Science and Engineering Center (DMR-2011967). XPS experiment was performed using instrumentation funded in part by the National Science Foundation Major Research Instrumentation Program under grant no. CHE-1338173. NMR experiment was performed by Dr. Philip Dennison at NMR facility at UCI Department of Chemistry.

References

1. P. Zou, Y. Sui, H. Zhan, C. Wang, H. L. Xin, H.-M. Cheng, F. Kang and C. Yang, *Chem. Rev.*, 2021, **121**, 5986-6056.
2. J. G. Zhang, W. Xu, J. Xiao, X. Cao and J. Liu, *Chem. Rev.*, 2020, **120**, 13312-13348.
3. T. Krauskopf, F. H. Richter, W. G. Zeier and J. Janek, *Chem. Rev.*, 2020, **120**, 7745-7794.
4. A. Manthiram, X. Yu and S. Wang, *Nat. Rev. Mater.*, 2017, **2**, 16103.
5. Q. Zhao, S. Stalin, C.-Z. Zhao and L. A. Archer, *Nat. Rev. Mater.*, 2020, **5**, 229-252.
6. T. Famprikis, P. Canepa, J. A. Dawson, M. S. Islam and C. Masquelier, *Nat. Mater.*, 2019, **18**, 1278-1291.

7. C. Wang, K. Fu, S. P. Kammampata, D. W. McOwen, A. J. Samson, L. Zhang, G. T. Hitz, A. M. Nolan, E. D. Wachsman, Y. Mo, V. Thangadurai and L. Hu, *Chem. Rev.*, 2020, **120**, 4257-4300 .
8. D. H. S. Tan, A. Banerjee, Z. Chen and Y. S. Meng, *Nat. Nanotechnol.*, 2020, **15**, 170-180.
9. M. Balaish, J. C. Gonzalez-Rosillo, K. J. Kim, Y. Zhu, Z. D. Hood and J. L. M. Rupp, *Nature Energy*, 2021, **6**, 227-239.
10. J. Wu, L. Shen, Z. Zhang, G. Liu, Z. Wang, D. Zhou, H. Wan, X. Xu and X. Yao, *Electrochem. Energy Rev.*, 2020, **4**, 101-135.
11. Y. Zhu, X. He and Y. Mo, *ACS Appl. Mater. Interfaces*, 2015, **7**, 23685-23693.
12. C. Zheng, J. Zhang, Y. Xia, H. Huang, Y. Gan, C. Liang, X. He, X. Tao and W. Zhang, *Small*, 2021, **17**, 2101326..
13. X. C. Chen, X. Liu, A. Samuthira Pandian, K. Lou, F. M. Delnick and N. J. Dudney, *ACS Energy Letters*, 2019, **4**, 1080-1085.
14. H. Duan, M. Fan, W. P. Chen, J. Y. Li, P. F. Wang, W. P. Wang, J. L. Shi, Y. X. Yin, L. J. Wan and Y. G. Guo, *Ad.v Mater.*, 2019, **31**, e1807789.
15. D. Y. Oh, Y. J. Nam, K. H. Park, S. H. Jung, K. T. Kim, A. R. Ha and Y. S. Jung, *Adv. Energy Mater.*, 2019, **9**, 1802927.
16. W. Zhou, S. Wang, Y. Li, S. Xin, A. Manthiram and J. B. Goodenough, *J. Am. Chem. Soc.*, 2016, **138**, 9385-9388.
17. L.-Z. Fan, H. He and C.-W. Nan, *Nat. Rev. Mater.*, 2021, **6**, 1003-1019.
18. J. Zhang, Y. Zhao, C. Chen, Y.-C. Huang, C.-L. Dong, C.-J. Chen, R.-S. Liu, C. Wang, K. Yan, Y. Li and G. Wang, *J. Am. Chem. Soc.*, 2019, **141**, 20118-20126.
19. H. Liu, Z. Zhu, Q. Yan, S. Yu, X. He, Y. Chen, R. Zhang, L. Ma, T. Liu, M. Li, R. Lin, Y. Chen, Y. Li, X. Xing, Y. Choi, L. Gao, H. S.-y. Cho, K. An, J. Feng, R. Kostecki, K. Amine, T. Wu, J. Lu, H. L. Xin, S. P. Ong and P. Liu, *Nature*, 2020, **585**, 63-67.
20. S. Li, Y.-M. Chen, W. Liang, Y. Shao, K. Liu, Z. Nikolov and Y. Zhu, *Joule*, 2018, **2**, 1838-1856.
21. Y. He, N. Liu and P. A. Kohl, *J. Electrochem. Soc.*, 2020, **167**, 100517.
22. M. J. Lee, J. Han, K. Lee, Y. J. Lee, B. G. Kim, K. N. Jung, B. J. Kim and S. W. Lee, *Nature*, 2022, **601**, 217-222.
23. Z. L. Brown, S. Jurng, C. C. Nguyen and B. L. Lucht, *ACS Appl. Energy Mater.*, 2018, **1**, 3057-3062.
24. Z. Lu, J. Yu, J. Wu, M. B. Effat, S. C. T. Kwok, Y. Lyu, M. M. F. Yuen and F. Ciucci, *Energy Storage Materials*, 2019, **18**, 311-319.
25. Y. Wang, C. J. Zanelotti, X. Wang, R. Kerr, L. Jin, W. H. Kan, T. J. Dingemans, M. Forsyth and L. A. Madsen, *Nat. Mater.*, 2021, **20**, 1255-1263.
26. Q. Zhang, A. B. Brady, C. J. Pelliccione, D. C. Bock, A. M. Bruck, J. Li, V. Sarbada, R. Hull, E. A. Stach, K. J. Takeuchi, E. S. Takeuchi, P. Liu and A. C. Marschilok, *Chem. Mater.*, 2017, **29**, 2364-2373.
27. H. Song, F. Liu and M. Luo, *Nano Research*, 2021, **14**, 814-822.
28. Q. Zhang, A. M. Bruck, D. C. Bock, J. Li, V. Sarbada, R. Hull, E. A. Stach, K. J. Takeuchi, E. S. Takeuchi and A. C. Marschilok, *Phys. Chem. Chem. Phys.*, 2017, **19**, 14160-14169.
29. T. Jiang and M. L. Falk, *Physical Review B*, 2012, **85**.
30. S. Wang, M. Yan, Y. Li, C. Vinado and J. Yang, *J. Power Sources*, 2018, **393**, 75-82.
31. W. D. Richards, L. J. Miara, Y. Wang, J. C. Kim and G. Ceder, *Chem. Mater.*, 2016, **28**, 266-273.
32. X. Hao, Q. Zhao, S. Su, S. Zhang, J. Ma, L. Shen, Q. Yu, L. Zhao, Y. Liu, F. Kang and Y. B. He, *Adv. Energy Mater.*, 2019, **9**, 1901604.
33. Q. Cheng, A. Li, N. Li, S. Li, A. Zangiabadi, T.-D. Li, W. Huang, A. C. Li, T. Jin, Q. Song, W. Xu, N. Ni, H. Zhai, M. Dontigny, K. Zaghib, X. Chuan, D. Su, K. Yan and Y. Yang, *Joule*, 2019, **3**, 1510-1522.
34. P. Hartmann, T. Leichtweiss, M. R. Busche, M. Schneider, M. Reich, J. Sann, P. Adelhelm and J. Janek, *The J. Phys. Chem. C*, 2013, **117**, 21064-21074.
35. X. Q. Zhang, X. B. Cheng, X. Chen, C. Yan and Q. Zhang, *Adv. Funct. Mater.*2017, **27**, 1605989.
36. Y. Lu, C. Z. Zhao, H. Yuan, X. B. Cheng, J. Q. Huang and Q. Zhang, *Adv. Funct. Mater.*, 2021, **31**, 2009925.